From Janus triboelectric interface to energy-autonomous sensing system: An asymmetric design☆

Lin Peng [a,b], Zhong Lin Wang [a,b,c,*,1], Xia Cao [b,d,**], Liqun Zhang [a,***]

[a] Beijing University of Chemical Technology, North Third Ring Road 15, Chaoyang District, Beijing 100029, China
[b] Beijing Institute of Nanoenergy and Nanosystems, Chinese Academy of Sciences, Beijing 101400, China
[c] School of Materials Science and Engineering, Georgia Institute of Technology, Atlanta, GA 30332–0245, United States
[d] Research Center for Bioengineering and Sensing Technology, Beijing Key Laboratory for Bioengineering and Sensing Technology, School of Chemistry and Biological Engineering, and Beijing Municipal Key Laboratory of New Energy Materials and Technologies, University of Science and Technology Beijing, Beijing 100083, China

ARTICLE INFO

ABSTRACT

The asymmetric and anisotropic conductive properties of Janus membranes is drawing considerable attention for the development of self-powered wearable electronics because it is a potential platform for endowing sustainable power sources such as triboelectric nanogenerator with high performance and multifunctionality. Herein, we prepared ultrathin electrically anisotropic Janus membranes by mixing liquid metal (LM) nanoparticles with a hydroxyethyl cellulose (HEC) suspension. The density deposited LM-HEC Janus film shows both excellent insulating properties on the HEC side and directly writable and conductive path properties on the LM side. A folding structured triboelectric nanogenerator (FS-TENG) was thus developed based on the insulating property of the HEC side for Morse code encrypted communication as well as Braille typewriters. Besides, a tactile sensor with visible light feedback functions was constructed using the functional circuit that was built on the conducting LM side, which promotes the design of wearable energy-autonomous sensing system by intrinsically integrating the self-power function with visual sensing parts. The simple preparation method applied in this study shed new light on the design and fabrication of flexible electronics that are based on Janus films.

1. Introduction

With the development of the Internet of Things (IOT) and wearable technology, the energy-efficient intelligent systems, which integrate energy harvesting devices with functional circuits by sharing basic parts, have become increasingly prominent in intelligent wearable flexible electronics. [1–3] Among the currently typical energy harvesting devices such as photovoltaics, [4,5] piezoelectric transducers, [6] triboelectric nanogenerators (TENGs), [7,8] or thermoelectric devices [9] and so on. TENGs have attracted increasing interest owing to their virtues of low cost, lightweight, high efficiency, and widespread applications in both power harvesting and environmental sensing fields.

[10–12].

At present, flexible circuits are generally built with polymer substrates and conductive materials such as metal films, graphene and conductive ink. For wearable applications, flexible circuits are required for matching the mechanical properties of natural soft tissues. [13–17] In this regard, flexible liquid metal (e.g., eutectic gallium indium alloy, EGaIn) offers a promising solution to develop flexible electronics and soft composites due to the low viscosity (2 mPa·s), high electrical conductivity (3.4×106 S·m−1), low melting point (< 15 ℃ for EGaIn) and low toxicity. [18,19] Up to date, liquid metal (LM) has been widely used to develop stretchable electrodes and flexible functional circuits in TENGs, which are usually composed of LM wrapped in a polymeric
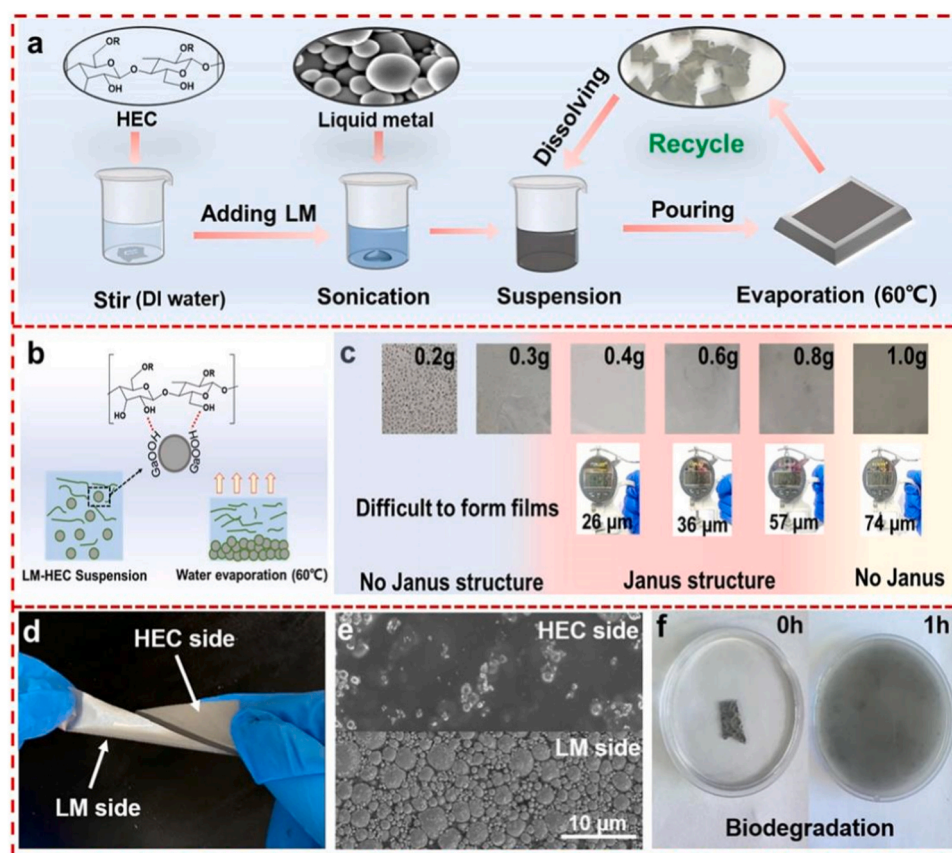
Fig. 1. Schematic illustration of the preparation process of LM-HEC Janus membrane (a) and the formation process of LM-HEC Janus films (b); (c) Impact of different masses of HEC on the morphology of the Janus films while maintaining the same mass of LM (2.0 g LM/40 mL water); (d) Photograph of the LM-HEC Janus film; (e) SEM images of different sides of the LM-HEC Janus film; (f) Biological degradation of LM-HEC Janus film in water.

material. [20,21] Thus, it inevitably suffers from complex processing steps and poor wettability due to the large surface tension of LM. As a comparison, the integration of LM with polymer materials can endow the composite with excellent electrical conductivity and more competitive mechanical properties. [22–24] Therefore, it may be more effective to utilize multifunctional liquid metal composites to improve the performance of TENGs.

Janus films, with its asymmetric structure and anisotropic electrical characteristics, have recently attracted increasing attention in various fields, such as energy storage/generation devices, [25,26] sensors/ actuators, [27–29] and thermal management. [30,31] Recently, Janus membranes have been used to prepare TENGs and have been shown to have high charge generation and charge trapping capabilities. [32,33] Typically, Janus functional films can be constructed by asymmetric fabrication (formation of Janus structures during film formation) and asymmetric modification (formation of Janus structures via post-modification). [34] Asymmetric fabrication strategies include continuous vacuum filtration [35] and phase separation. [36,37] Meanwhile, asymmetric modification strategies can be achieved by surface modification [38] and surface chemical self-assembly. [39,40] However, most of the above strategies suffer from time-consuming multi-step processes and low production efficiency. [41,42] Hence, it is urgent to develop a highly efficient and mass-produced method for the preparation of Janus functional films for practical applications.

Thus, in this work, flexible Janus films with electrically conductive anisotropy are developed via a simple self-assembly density deposition method, where ultrathin and highly flexible composite material is obtained by the self-assembly of micro/nanodroplets of EGaIn alloy with hydroxyethyl cellulose (HEC). After erasing and etching in the LM nanoparticles-rich side (LM side), the conducting circuits were

constructed by direct writing technology on LM side. A folding structured triboelectric nanogenerator (FS-TENG) with the insulated side (HEC side) of Janus membrane is fabricated for self-powered sensors and applied to Morse code encrypted communication as well as Braille typewriters. Moreover, a tactile sensor with visible light feedback functions is constructed using this Janus membrane, where the intrinsic asymmetric conducting property of the Janus films promotes the design of energy-autonomous sensing system by effectively integrating the TENG-based energy harvesting function with the visual sensing module. The as-prepared multifunctional and recyclable LM-HEC Janus films present a new sustainable and adaptive extension strategy toward efficient and environmentally friendly self-powered multifunctional systems.

2. Material and methods

2.1. Fabrication of the LM-HEC Janus film

HEC powder (Aladdin) was dissolved in 40 mL of DI water and stirred for 10 min at room temperature. EGaIn alloy (melting point of 15.8 ℃) was purchased from Hunan ShengTe New Materials Co., ltd. China. A specific quantity of LM was dropped into the HEC solution and dispersed with probe ultra-sonication for 12 min to obtain the uniform LM-HEC suspension. Then, the suspension was stirred for 10 min at 60 °C. Subsequently, The prepared suspension was cast in a PMMA mold for 4 h (at 60 °C) to be dried. The LM-HEC Janus film was obtained after complete evaporation of water.
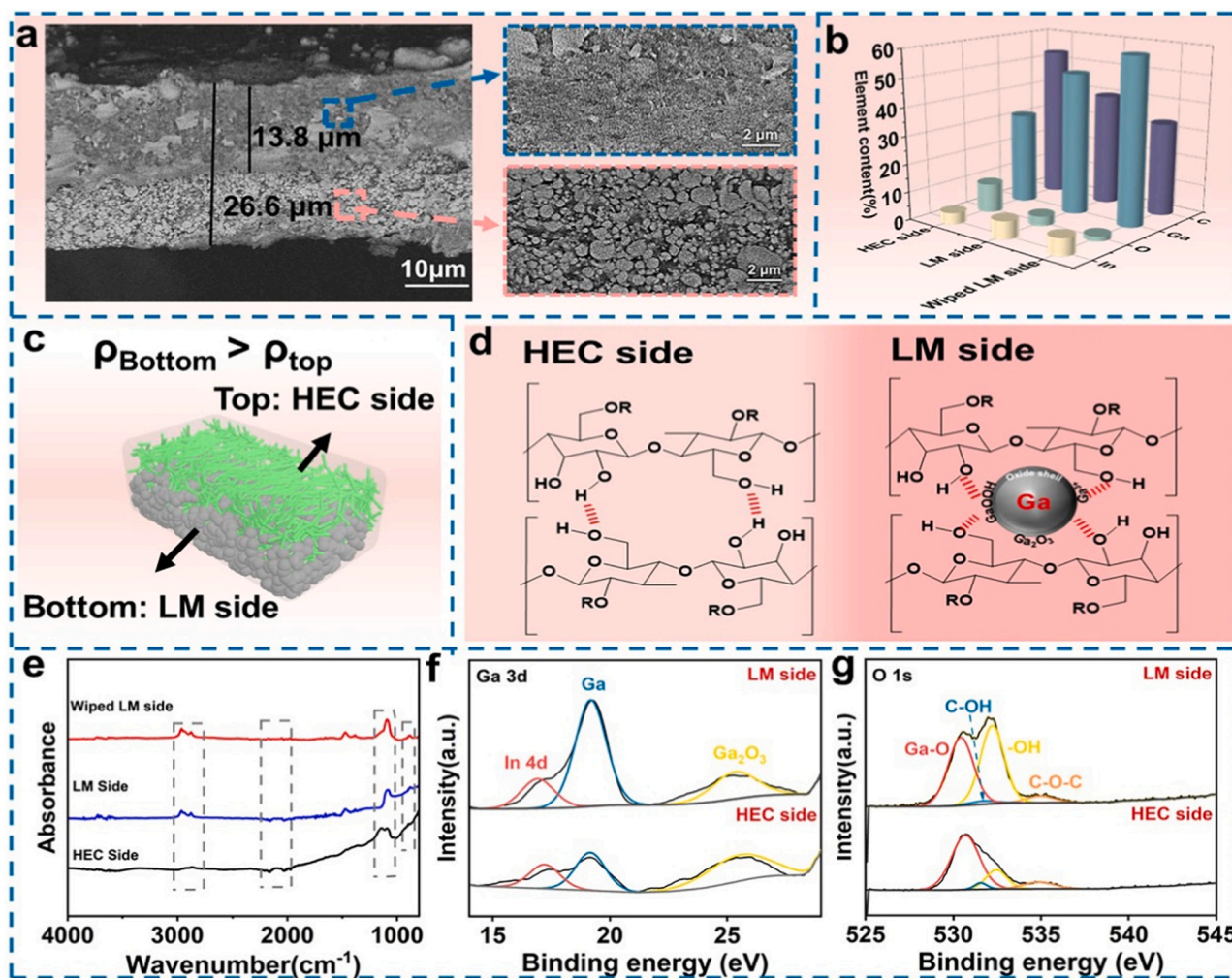
Fig. 2. (a) SEM image of the cross section of the LM-HEC Janus film. Scale bar: 10 μm. Top right inset shows the enlarged SEM image of the upper layer. The lower right inset shows the enlarged SEM image of the lower layer. Scale bars: 2 μm. (b) The content difference of C, Ga, O and In elements on the HEC side, LM side and wiped LM side of the film. (c) Schematics of the cross sections of the LM-HEC Janus film. (d) Possible self-assembly mechanisms of HEC side and LM side of the LM-HEC Janus film. (e) FTIR curves of HEC side, LM side and wiped LM side. (f) XPS spectra of Ga 3d of the LM side and HEC side of the LM-HEC Janus film. (h) XPS spectra of O 1 s of the LM side and HEC side of the LM-HEC Janus film.

2.2. Characterization and Measurement

The surface morphology of LM-HEC Janus film was characterized using a Nova Nano450 scanning electron microscope (SEM). X-ray photoelectron spectroscope (Thermo Scientific K-Alpha) was used to get XPS spectra of the corresponding samples. FTIR data were obtained by a Nicolet iS10 FT-IR spectrometer. The resistance was recorded using the digital multimeter (DM3068). The electrical outputs of the TENG were collected by potentiometers (Keithley 6514 system).

3. Results and discussion

The self-assembly fabrication of liquid metal- hydroxyethyl cellulose (LM-HEC) Janus films are schematically shown in Fig. 1a. It can be seen that Janus films are obtained from LM and HEC by a simple density deposition method. Fig. 1b illustrates the principle of film formation, where HEC not only serves as a dispersant to stabilize the EGaIn LM droplets, but also as a binder to link LM particle together to form a dense film. Due to the dispersal effect of HEC, liquid metal nanoparticles can efficiently maintain a granular state and avoid aggregation. Since the density of liquid metal is much higher than that of HEC, the particles sink to the bottom during the evaporation of the suspension, thus forming this Janus film through self-assembly in the density deposition

process. Fig. 1c shows the variation of the LM side of the Janus film with different content of HEC, and it can be seen that the Janus structure can be formed when HEC content is between 0.4 and 0.8 g. Below 0.4 g, it's difficult for forming the Janus film. Above 1 g, LM cannot be effectively deposited to present the Janus characteristics, and the thickness of the film increases with the increase of HEC. As shown in Fig. 1d, HEC with black color mainly constitutes the top surface, while LM, which has a silver color, mainly deposited on the bottom surface. Fig. 1e shows the two sides of the membrane, the bottom (LM side) is composed of piled liquid metal particles, while the top (HEC side) is formed by HEC to form a more uniform membrane. Fig. 1f shows the degradable properties of the membrane, which can be restored to suspension in one hour after being placed in aqueous solution.

To further understand the formation mechanism of Janus membrane, two sides of the Janus membrane were characterized in more detail. Fig. 2a shows the SEM image of the cross-section of the LM-HEC Janus film, which shows obvious stratification, and the LM micro/nanodroplets are mainly distributed in the lower layer and stacked together one by one. The energy spectrum of elements on the HEC side, LM side, and wiped LM side are shown in Fig. 2b. It can be seen that the distribution of C content is HEC side > LM side > wiped LM side, while the distribution of Ga element content is wiped LM side > LM side > HEC side, verifying that the denser liquid metal is mainly distributed in the
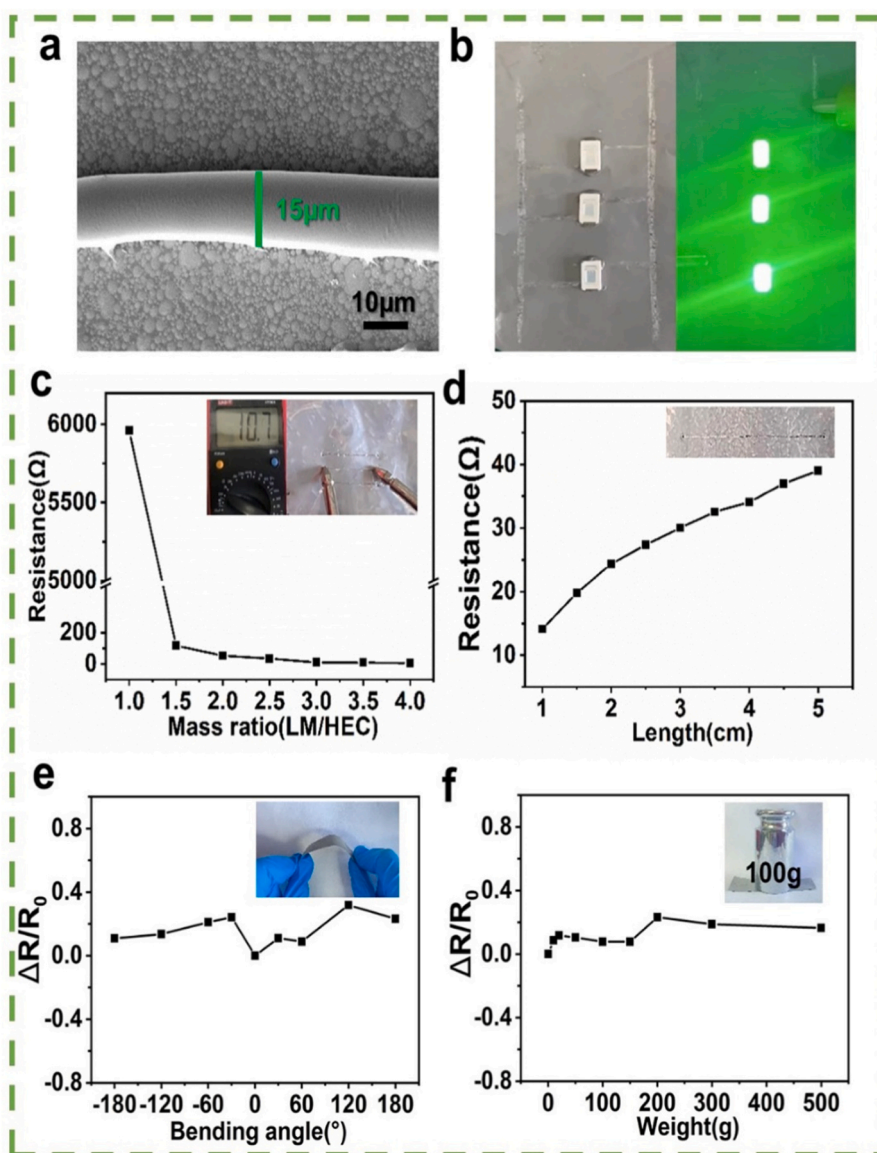
Fig. 3. (a) SEM images of the conductive lines obtained by applying shear friction on the LM side of LM-HEC Janus films. (b) Photograph of an interdigital circuit on the LM side constructed by a writing method; an LED array in the circuit is lit up. (c) Resistance of different LM/HEC mass ratio of the wiped path. (d) Resistance of different writing length of the wiped path. (e) Resistance changes of the wiped path at different bending angles from − 180–180°. (f) Resistance changes of the wiped path under different weights.

lower layer of the film. Fig. 2c schematically simulates this hierarchical structure. Owing to the different density of LM and HEC, LM particles are mainly deposited at the bottom, thus forming Janus structure. Fig. 2d depicts the process of Janus membrane self-assembly formation, the upper HEC side is mainly formed by the hydrogen bonding interaction between hydroxyethyl cellulose -OH self-assembly. The formation of the lower LM side mainly stems from the presence of the layer of metal oxide (GaOOH/Ga2O3) on the liquid metal surface, and the -OH group on HEC can form hydrogen bonds with Ga3 + and GaOOH (Fig. 2c). Here the interaction and coordination can stabilize the distribution of liquid metal micro/nanodroplets in the composite. It can be seen from Fig. S1 that the LM-HEC suspension is more stable after the addition of HEC compared with the aqueous LM solution, and the suspension remains stable after one day of resting without dispersion. HEC prevents the agglomeration of LM nanoparticles due to the binder functions of the polymer. The FTIR spectroscopy measurements are performed on the HEC side, LM side, and wiped LM side to investigate the electrostatic interactions between HEC and LM nanoparticles, and

the results are shown in Fig. 2e. The absorption peaks at 2932–2862 cm− 1 account for the presence of stretching vibrations of –OH and –CH bonding in the HEC polymer. [43,44] The absorption bands at 1186 cm− 1 represent the C–O bond stretching, while the band at 1049 cm− 1 shows the deformation of the O–H bond and the bands in the fingerprint region are due to C–H bond bending vibrations. [45,46] The disappearance of C–H stretching and narrowing of O–H stretching in LM side and wiped LM side spectrum confirm the involvement of these groups in metal coordination and hydrogen bond formation. [47,48] The bands at 2177 and 2048 cm− 1 also disappeared, and this indicates the oxidation of hydroxyl groups of the HEC polymer. The peak corresponding to the stretching vibration of the Ga–O bond is observed at 870 cm− 1. [49] It is assumed that cellulose decorates LM surface and provides plentiful functional groups.

X-ray photoelectron spectroscopy (XPS) analysis of the different surfaces of Janus membranes is also performed. The XPS Ga 3d spectrum is shown in Fig. 2f, three obvious peaks can be found. The characteristic peaks at around 16.8 eV, 19.0 eV, and 25.3 eV are assigned to In 4d, Ga
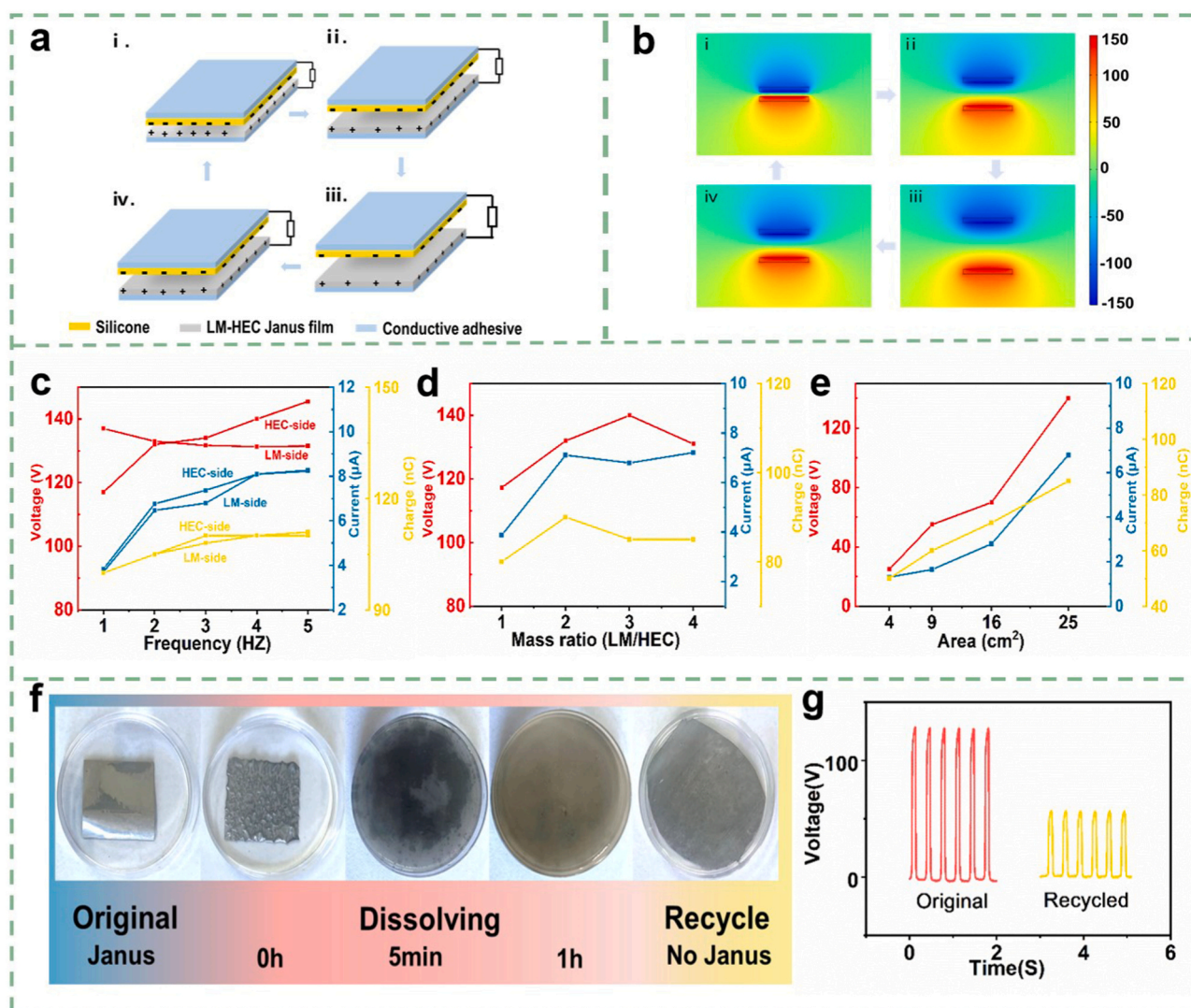
Fig. 4. (a) Schematic diagram of the working principle for the LH-TENG in contact-separation mode. (b) Simulated potential distributions of the LH-TENG through the COMSOL Multiphysics. (c) Comparison of voltage, current and charge of different side of LM-HEC Janus films at different frequencies. (d) Output performance of LM-HEC Janus film with different LM/HEC mass ratios and (e) different area. (f) Degradation Process of LM-HEC Janus film. (g) Output voltage of original and recycled films.

and Ga_2O_3, respectively. [50] It can be seen that the peak of Ga on the LM side is higher than that on the HEC side, confirming the higher LM content on the LM side. Notably, the peak of Ga_2O_3 shifts to high binding energy compared to Ga_2O_3 peaks in previous studies, which results from hydrogen-bonding interactions between LM and HEC [51]. The XPS O 1 s spectra are shown in Fig. 2g, the peak at 530.38 eV, 531.68 eV, 532.18 eV, and 534.88 eV are attributed to Ga-O, C-OH, -OH, and C-O-C, respectively. [52] We observed that the peak of -OH on the LM side is significantly higher than that on the HEC side, presumably because Ga generates GaOOH during the sonication process, which leads to more hydroxyl due to the accumulation of more Ga nanoparticles on the LM side. [53]

Shear friction on LM side of Janus film can destroy the oxide layers on LM droplets and allow the droplets to locally and spontaneously coalesce and then form the desired electrical conduction routes (Figure S4). The yield conductive path (about 15 μm) is shown in Fig. 3a. An interdigital circuit was constructed on the Janus film by the writing method, and an LED array connected in the circuit could be lit up, as presented in Fig. 3b and Movie S1. The corresponding equivalent circuit powering the LED array is shown in Figure S5. According to the previously reported method, where liquid metal is directly used as conductive ink, the large surface tension and easy oxidation of liquid metal lead to the difficulty and instability of the conductive path. In contrast, shear friction is only imposed on the outer layer of the LM particle, which can easily produce a smooth and precise conductive channel. The conductivity of the films prepared with different contents of LM and HEC were investigated and it was found that the conductivity of the films stabilized after the LM/HEC was higher than 1.5 (Fig. 3c).

Supplementary material related to this article can be found online at doi:10.1016/j.nanoen.2023.109146.

Therefore, the films with a mass ratio of 2 between LM and HEC were chosen for the conductivity stability study. Fig. 3d shows the change in resistance of the conducting path after inscribing different lengths of paths. It can be seen that the longer the path length, the higher the resistance and the worse the conductivity. The electrical property of the conductive pathways by the developed wiping method is very stable. As shown in Fig. 3e, the change in resistance is less than 0.4 when the film is bent to different angles. Fig. 3f shows the resistance change when loading different weights on the film.

The asymmetric feature of the Janus film enables its triboelectric operation for self-powered integrated sensing systems. The triboelectrically properties of a single Janus membrane were first
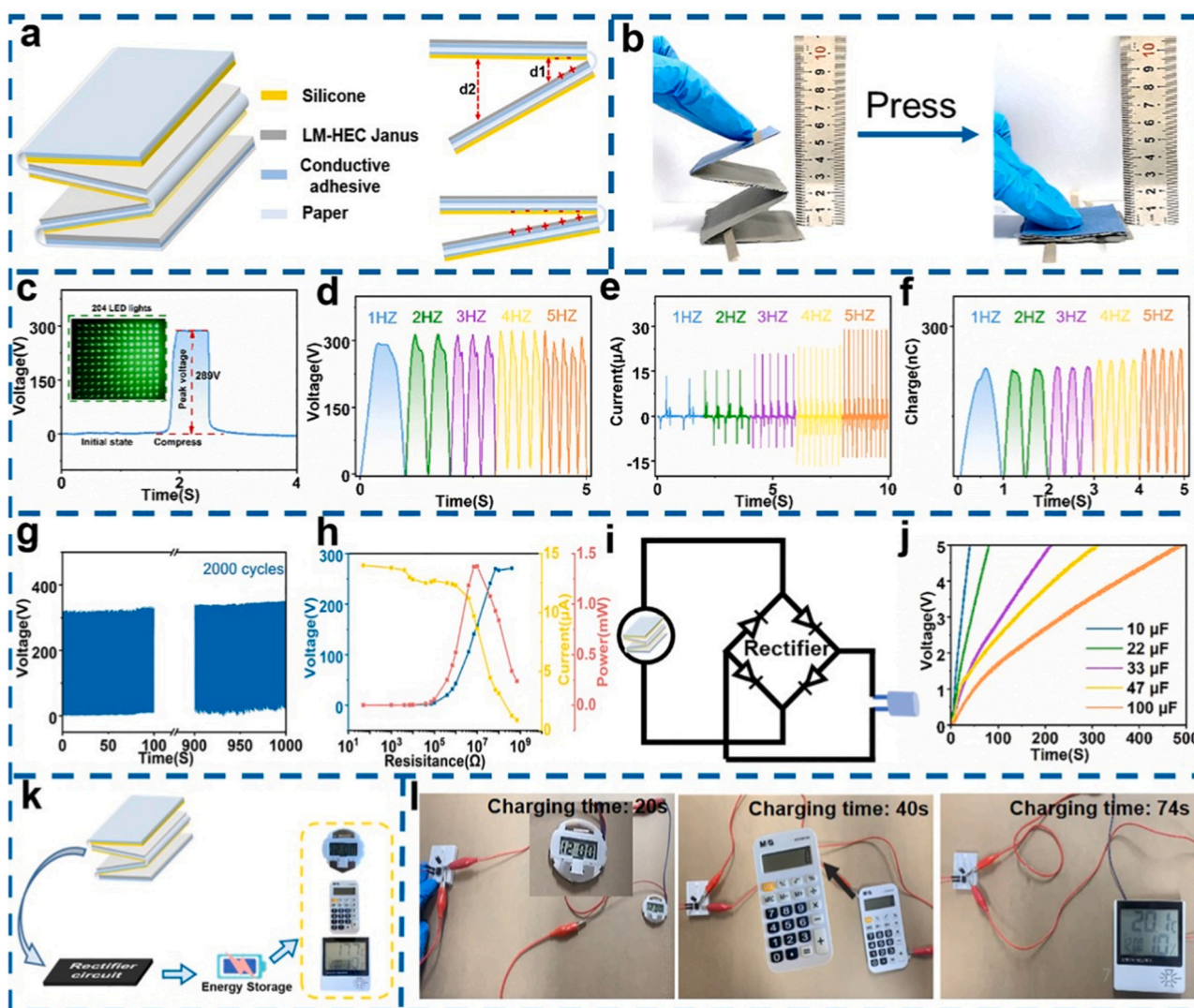
Fig. 5. (a) The basic structure of FS-TENG. (b) The digital photos of FS-TENG stretched and compressed. (c) The open-circuit voltage for one working process of FS-TENG; the inset illustrations show the FS-TENG (area: 5 *5 cm) driving 204 LEDs. (d-f) Electrical output of the FS-TENG. (g) Output voltage stability of the FS-TENG. (h) Output voltage, output current and output power of FS-TENG at different load resistances. (i) Charging circuit diagram after rectification. (j) Charging commercial capacitors by the FS-TENG. (K) FS-TENG circuit diagram with power supply for different electronic devices. (l) Image of a watch, calculator, and hygrometer successfully powered by charging a capacitor of 33μF using FS-TENG at 3HZ.

characterized. A flexible contact-separation mode LH-TENG was designed after the Janus film served as the positive friction material. Fig. 4a shows the contact-separation mode of LH-TENG for electricity-generation. Silicone is selected as the negative friction material to contact with the Janus film throughout the experiments. The generation of triboelectricity depends on the electronegativity difference between two friction materials. When the silicone is touched by the LM-HEC Janus film in the original mode, charges are generated due to tribo-electrification between the silicone and LM-HEC Janus film with equally opposite polarities distributed on their surface (Fig. 4a(i)). In Fig. 4a(ii), when the force pressed on LH-TENG is unloaded, a potential difference is formed after the LM-HEC Janus film and the silicone film are separated. The current direction is shown in the diagram. When the distance be-tween the two surfaces increases gradually, the open circuit voltage between LH-TENG increases gradually. Until Fig. 4a(iii), the LH-TENG voltage reaches the maximum and is in a saturated state. When the pressure is reapplied, the distance between silicone and LM-HEC Janus film in Fig. 4a(iv) is closing, the potential between the two electrodes gradually disappeared, and the open circuit voltage gradually decreased from the maximum until it returned to Fig. 4a(i) state again, and the

voltage value was zero. The induced triboelectric potential distributions can be readily simulated by COMSOL employing finite element analysis (Fig. 4b). When silicone and LM-HEC Janus film fully contacted, the potential difference between two aluminum electrodes was minimum. With the release of LH-TENG external force, the potential difference increased gradually due to triboelectrification and electrostatic effect, until the saturation state. When the pressure was applied again, the potential difference will decrease. This simulation perfectly conforms to the actual working state of LH-TENG. Figure S6–8 using six different friction layers for comparative testing, measurement of LH-TENG output performance comparison. Among them, the open-circuit voltage, short-circuit current and transfer charge corresponding to silicone are the largest, with the voltage up to 150 V, the short-current up to 12.5 μA and the transfer charge of 95 nC. This is because silicone is more likely to gain electrons than other materials and has the largest electronegativity difference with the LM-HEC Janus films. Fig. 4c shows the open-circuit voltage, short-circuit current and transferred charge of different side of Janus membrane at different frequencies. The average open-circuit voltage and short-circuit current and transferred charges of HEC side is slightly higher than those of the LM side. Figure S9–14 shows the
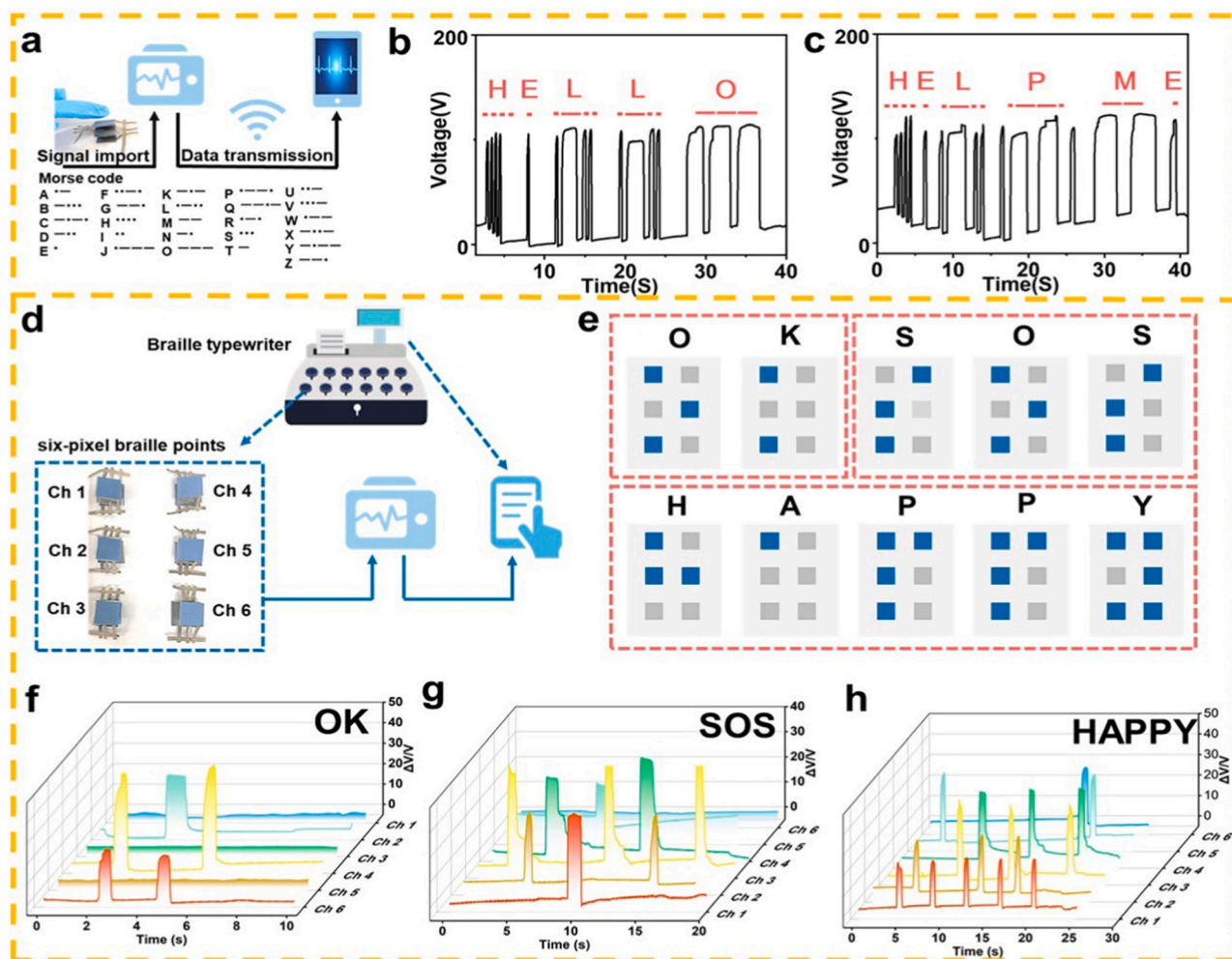
Fig. 6. (a) Schematic illustration of the wireless transmission system and the related symbols of the international Morse codes in the alphabet. (b) The practical applications of FS-TENG (area: 2 *2 cm) to recode and transmit the greeting signal of "HELLO". (c) The practical applications of FS-TENG to recode and translate the distress signal of "HELP ME". (d) Schematic design of a Braille typewriter. (e) Braille mapping of English alphabets, where blue points and grey points represent convex points and flat points, respectively. Real-time recording of multi-channel resistance changes to convey different Braille signals such as f) "OK", g) "SOS", and h) "HAPPY".

detailed output performance data. By comparison, we finally chose HEC side as the positive friction layer in this study. Fig. 4d shows the comparison of voltage, current, and charge output of LH-TENG using LM-HEC Janus films with different mass ratios of LM and HEC, and it can be seen that when LM/HEC= 3, the output voltage of TENG reaches the maximum with 140 V; the current and charge level off and change less after LM/HEC> =2. Fig. 4e shows the comparison of voltage, current, and charge output of LH-TENG for different areas of Janus membrane, and it can be seen that the voltage, current, and charge intensity all increased with the increase of membrane area. Since the membranes have recyclable degradation properties, the triboelectric properties of the degraded and re-formed membranes were characterized. Fig. 4f shows the detailed membrane degradation and reformation process. Janus membrane became crumpled immediately upon exposure to water, broke up after 5 min of dissolution, and reformed a uniform suspension after 1 h of dissolution. Notably, the reformed membrane no longer has the original Janus structure, probably due to the irreversible disruption of the hydrogen bonding between HEC and LM. We tested the voltage (Fig. 4g), current (Figure S15) and charge (Figure S16) changes of TENG assembled with different membranes before and after degradation, and it can be seen that the output performance of degraded membranes without Janus structure is much reduced, which reflects that Janus structure plays an important role in improving the output

performance.

Device miniaturization represents a trend in the development of flexible wearable devices, though simply reducing the area of the device will reduce the output performance of the device. Therefore, a folding structured triboelectric nanogenerator (FS-TENG) was designed to improve the tribological area of the TENG through origami technology which integrates six tribological surfaces into a single FS-TENG (Fig. 5a). The equivalent circuit models of FS-TENG with different parallel connections among triboelectric cells are shown in Figure S17. Fig. 5b shows the contact-separation process of this FS-TENG. It can be seen that the whole device is very lightweight and can be extended or compressed by 10 times (60 mm/6 mm). Owing to the origami technology, the FS-TENG with a size of 5 cm × 5 cm generated an open-circuit voltage up to 289 V and could light up 204 LEDs (Fig. 5c). Fig. 5(d-f) show the open-circuit voltage, short-circuit current and transfer charge of FS-TENG at different frequencies. And the open-circuit voltage and transfer charge are relatively stable. The current increases with the increase of frequency. Durability and stability are two important characteristics that affect the practical application of TENG. The long-term operating capability of the FS-TENG is examined by testing its output voltage for 2000 cycles. Fig. 5g displays that the voltage remains essentially constant after continuous operation and the output is not degraded. Fig. 5h show that as the external resistance value increased from 1 MΩ to
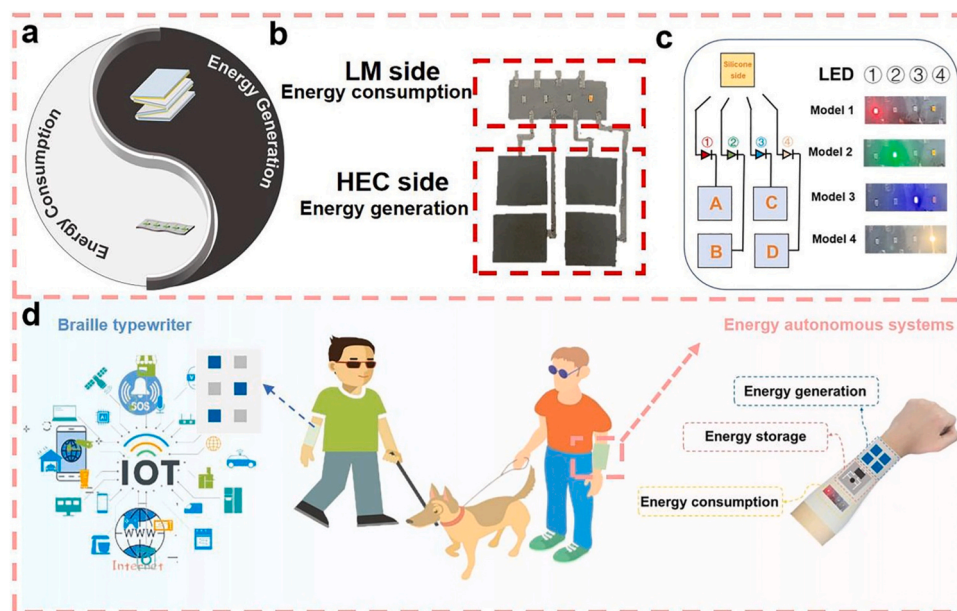
Fig. 7. (a) Schematic diagram of the functional demonstration of the Janus membrane. (b) Wearable visual tactile sensors. (c) Feedback mechanisms for wearable visual tactile sensors. (d) A schematic of wearable self-powered sensor integrated a Braille typing system and an energy autonomous system for Deafblind Assistance.

1000 MΩ, the peak value of output current decreased and the peak value of output voltage increased gradually, while the output power first increased and then decreased. When the resistance value was adjusted to 70 MΩ, the power reached the maximum value of 1369 μW. The standard charging capacity of the FS-TENG is characterized by using it to charge commercial capacitors (10, 22, 33, 47 and 100μF) under high frequency (3 Hz) excitation. A rectifier is introduced into the circuit to convert the alternation current into direct current (Fig. 5i). As plotted in Fig. 5j, it takes 479 s to charge the capacitor of 100μF to 5 V, but it only takes 39 s to charge the 2.2 μF capacitor to 5 V. Utilizing the collected power of the capacitor to drive all kinds of electronic components, and its diagram is demonstrated in Fig. 5k. Fig. 5l shows the capacitor successfully driving the watch, calculator and hygrometer after FS-TENG charged the capacitor.

To demonstrate the potential applications of the as-designed FS-TENG for tactile sensing and human-computer interaction, a Morse code communicator and a Braille typewriter were prepared using FS-TENG. Morse code, as a way to transmit various kinds of information, has been used for more than a century. It consists of "dots" and "dashes", and represents different Latin alphabet through different arrangements (Fig. 6a).

For practical applications, the"dots" and "dashes" are transformed into visual voltage signals in real-time. For instance, the greeting signals of "HELLO" (Fig. 6b) and the distress signals of "HELP ME" (Fig. 6c) were recorded by pressing a FS-TENG with a size of 2 cm × 2 cm rhythmically with different duration times. The excellent performance of the as-designed FS-TENG also inspired the further exploration as intelligent interfaces to facilitate electrical signal-based information communication between humans and machines, leading to the fabrication of a Braille typewriter for the visually impaired.(Fig. 6 d) Braille is a tactile script designed for the blind. Generally, each square of braille is made up of six dots, 123 from top to bottom on the left and 456 on the right.(Fig. 6 e) The design concept here is to use an array composed of six FS-TENG to match the Braille cell, known as, six-pixel Braille points. Each Braille dot corresponded to a channel signal (e.g. Ch1) and recorded the voltage signal change of the channel. Thus, as a proof-of-concept, different Braille patterns such as "OK", "SOS", and "HAPPY" can be successfully input and transmitted according to the varying voltage change of each channel (Fig. 6f-h).

The double-layer feature of the LM-HEC Janus film enables it to operate as multifunctional wearable devices on the basis of the TENG principle. Fig. 7a schematically presents the characterization of the Janus film. Fig. 7b and Movie S2 show a wearable visual tactile sensor based on the double-layer properties of Janus membrane. The HEC side is served as the TENG based self-powered tactile sensor, and a circuit is built on the LM side as the TENG side optical feedback. Fig. 7c illustrates the feedback mechanism of this wearable visual tactile sensor. When we press the different modules (A,B, C, D) on HEC side with silicone contact, the corresponding lamps in series can be lighten. As a result, the Janus membrane has a promising application in human wearable devices. Fig. 7d is A schematic of wearable self-powered sensor integrated a Braille typing system and an energy autonomous system for Deafblind Assistance.

Supplementary material related to this article can be found online at doi:10.1016/j.nanoen.2023.109146.

4. Conclusion

In summary, a multifunctional, recyclable and flexible Janus film was developed by using the self-assembly effect between LM and HEC in the density deposition process. A TENG with a folding structure (FS-TENG) was developed based on the insulating HEC side, which can be utilized for Morse code disguised communication by constructing a six-pixel Braille typewriter. Also, by utilizing direct write technology, a conductive path was formed directly on the LM side by shear erasure, based on which a tactile sensor with visible light feedback functions and a wearable energy-autonomous sensing system were constructed. Finally, we describe a wearable self-powered sensor integrated with a Braille typing system and an energy autonomous system for Deafblind Assistance. This work demonstrates the great potential of design of multifunctional TENGs on the base of asymmetric platforms for applications such as wearable flexible sensors, electronic skins and humanoid robotics, etc.

CRediT authorship contribution statement

Lin Peng: Conceptualization, Supervision, Writing – original draft. Zhong Lin Wang: Conceptualization, Funding acquisition, Supervision, Writing – review & editing. **Xia Cao:** Conceptualization, Funding acquisition, Supervision, Writing – review & editing. **Liqun Zhang:**

Conceptualization, Supervision, Writing – review& editing.

Declaration of Competing Interest

The authors declare that they have no known competing financial interests or personal relationships that could have appeared to influence the work reported in this paper.

Data Availability

Data will be made available on request.

Notes

The authors declare no competing financial interest.

Appendix A. Supporting information

Supplementary data associated with this article can be found in the online version at doi:10.1016/j.nanoen.2023.109146.

References

[1] B. Shi, Z. Liu, Q. Zheng, J. Meng, H. Ouyang, Y. Zou, D. Jiang, X. Qu, M. Yu, L. Zhao, Y. Fan, Z.L. Wang, Z. Li, ACS Nano 13 (2019) 6017–6024.
[2] J. Yang, J. Cao, J. Han, Y. Xiong, L. Luo, X. Dan, Y. Yang, L. Li, J. Sun, Q. Sun, Nano Energy 101 (2022), 107582.
[3] Y. Zhang, L. Wang, L. Zhao, K. Wang, Y. Zheng, Z. Yuan, D. Wang, X. Fu, G. Shen, W. Han, Adv. Mater. 33 (2021) 2170174.
[4] P. Huen, W.A. Daoud, Renew. Sustain. Energy Rev. 72 (2017) 1295–1302.
[5] S. Kim, M. Patel, T.T. Nguyen, N. Kumar, P. Bhatnagar, J. Kim, ACS Appl. Mater. Interfaces 14 (2022) 706–716.
[6] J.H. Lee, J.Y. Park, E.B. Cho, T.Y. Kim, S.A. Han, T.H. Kim, Y. Liu, S.K. Kim, C. J. Roh, H.J. Yoon, H. Ryu, W. Seung, J.S. Lee, J. Lee, S.W. Kim, Adv. Mater. 29 (2017), 1606667.
[7] Z. Deng, L. Xu, H. Qin, X. Li, J. Duan, B. Hou, Z.L. Wang, Adv. Mater. 34 (2022), e2205064.
[8] Z. Huo, Y. Wei, Y. Wang, Z.L. Wang, Q. Sun, Adv. Funct. Mater. 32 (2022), 2206900.
[9] S. El Oualid, I. Kogut, M. Benyahia, E. Geczi, U. Kruck, F. Kosior, P. Masschelein, C. Candolfi, A. Dauscher, J.D. Koenig, A. Jacquot, T. Caillat, E. Alleno, B. Lenoir, Adv. Energy Mater. 11 (2021) 2170073.
[10] Y. Zhou, M. Shen, X. Cui, Y. Shao, L. Li, Y. Zhang, Nano Energy 84 (2021), 105887.
[11] J. Zhu, Y. Cheng, S. Hao, Z.L. Wang, N. Wang, X. Cao, Adv. Funct. Mater. 31 (2021), 2100039.
[12] Z.L. Wang, Adv. Energy Mater. 10 (2020) 2000137.
[13] Y. Wang, H. Guo, J.J. Chen, E. Sowade, Y. Wang, K. Liang, K. Marcus, R. R. Baumann, Z.S. Feng, ACS Appl. Mater. Interfaces 8 (2016) 26112–26118.
[14] G. Long, W. Jin, F. Xia, Y. Wang, T. Bai, X. Chen, X. Liang, L.M. Peng, Y. Hu, Nat. Commun. 13 (2022) 6734.
[15] L. Teng, S. Ye, S. Handschuh-Wang, X. Zhou, T. Gan, X. Zhou, Adv. Funct. Mater. 29 (2019), 1808739.
[16] X. Zhou, W. Guo, P. Peng, Nanomicro Lett. 13 (2021), 184.
[17] W. Gao, H. Ota, D. Kiriya, K. Takei, A. Javey, Acc. Chem. Res. 52 (2019) 523–533.
[18] J. Ma, F. Krisnadi, M.H. Vong, M. Kong, O.M. Awartani, M.D. Dickey, Adv. Mater. (2022), e2205196, https://doi.org/10.1002/adma.202205196.
[19] T. Daeneke, K. Khoshmanesh, N. Mahmood, I.A. de Castro, D. Esrafilzadeh, S. J. Barrow, M.D. Dickey, K. Kalantar-Zadeh, Chem. Soc. Rev. 47 (2018) 4073–4111.
[20] L.E. Helseth, Nano Energy 50 (2018) 266–272.
[21] C. Yang, J. He, Y. Guo, D. Zhao, X. Hou, J. Zhong, S. Zhang, M. Cui, X. Chou, Mater. Des. 201 (2021), 109508.
[22] Q. Ye, Y. Wu, Y. Qi, L. Shi, S. Huang, L. Zhang, M. Li, W. Li, X. Zeng, H. Wo, X. Wang, S. Dong, S. Ramakrishna, J. Luo, Nano Energy 61 (2019) 381–388.
[23] C. Pan, D. Liu, M.J. Ford, C. Majidi, Adv. Mater. Technol. 5 (2020), 2000754.
[24] Z. Sha, C. Boyer, G. Li, Y. Yu, F.-M. Allioux, K. Kalantar-Zadeh, C.-H. Wang, J. Zhang, Nano Energy 92 (2022), 106713.
[25] J.-L. Wang, S.-H. Yu, Matter 1 (2019) 1110–1111.
[26] Z. Song, W. Li, Y. Bao, W. Wang, Z. Liu, F. Han, D. Han, L. Niu, Adv. Electron. Mater. 4 (2018), 1800252.
[27] J.N. Ma, J.W. Mao, D.D. Han, X.Y. Fu, Y.X. Wang, Y.L. Zhang, Adv. Mater. Technol. 4 (2019) 1900554.
[28] B. Liu, M. Taheri, J.F. Torres, Z. Fusco, T. Lu, Y. Liu, T. Tsuzuki, G. Yu, A. Tricoli, ACS Nano 14 (2020) 13852–13864.
[29] Y. Xie, Q. Ma, B. Yue, X. Chen, Y. Jin, H. Qi, Y. Hu, W. Yu, X. Dong, H. Jiang, Chem. Eng. J. 452 (2023), 139393.
[30] X. Yue, T. Zhang, D. Yang, F. Qiu, G. Wei, H. Zhou, Nano Energy 63 (2019), 103808.
[31] P. Yang, J. He, Y. Ju, Q. Zhang, Y. Wu, Z. Xia, L. Chen, S. Tang, Adv. Sci. (Weinh.) 10 (2023), e2206176.
[32] Y. Xie, Q. Ma, H. Qi, X. Liu, X. Chen, Y. Jin, D. Li, W. Yu, X. Dong, Nanoscale 13 (2021) 19144–19154.
[33] Y. Xie, Q. Ma, B. Yue, X. Chen, Y. Jin, H. Qi, Y. Hu, W. Yu, X. Dong, H. Jiang, Chem. Eng. J. 452 (2023), 139393.
[34] H.C. Yang, Y. Xie, J. Hou, A.K. Cheetham, V. Chen, S.B. Darling, Adv. Mater. 30 (2018), e1801495.
[35] C.-M. Kim, S. Hong, R. Li, I.S. Kim, P. Wang, ACS Sustain. Chem. Eng. 7 (2019) 7252–7259.
[36] Y. He, X. Wang, Y. He, X. Zhao, J. Lin, Y. Feng, J. Chen, F. Luo, Z. Li, J. Li, H. Tan, J. Mater. Chem. B 10 (2022) 2602–2616.
[37] Y. Liu, T. Xiao, C. Bao, Y. Fu, X. Yang, J. Membr. Sci. 563 (2018) 298–308.
[38] Y. Liang, J. Shi, P. Xiao, J. He, F. Ni, J. Zhang, Y. Huang, C.F. Huang, T. Chen, Chem. Commun. (Camb.) 54 (2018) 12804–12807.
[39] J. Bai, Z. Shi, J. Yin, M. Tian, R. Qu, Adv. Funct. Mater. 28 (2018), 1800939.
[40] B. Zhang, Q. Gu, C. Wang, Q. Gao, J. Guo, P.W. Wong, C.T. Liu, A.K. An, ACS Appl. Mater. Interfaces 13 (2021) 3762–3770.
[41] X. Yang, L. Yan, F. Ran, A. Pal, J. Long, L. Shao, J. Membr. Sci. 576 (2019) 9–16.
[42] F. Tang, S. Li, H.-Y. Yu, C. Wang, Y. Li, Z. Li, J. Yao, J. Tang, J. Zhu, ACS Sustain. Chem. Eng. 8 (2020) 17458–17465.
[43] I. Hussain, X. Ma, L. Wu, Z. Luo, Cellulose 29 (2022) 5725–5743.
[44] C. Jo, B. Rukmanikrishnan, P. D. S, S. Ramalingam, J. Lee, ACS Sustain. Chem. Eng. 9 (2021) 13653–13662.
[45] Z. Lu, J. Huang, S. E, J. Li, L. Si, C. Yao, F. Jia, M. Zhang, Carbohydr. Polym. 250 (2020), 116919.
[46] N. Sun, T. Wang, X. Yan, RSC Adv. 7 (2017) 9500–9511.
[47] A.S.A. Alsubaie, D. Lu, J. Spectro 2022 (2022) 1–9.
[48] Y.-x Zhang, X.-y Guo, B. Liu, J.-l Zhang, X.-h Gao, Q.-x Ma, S.-b Fan, T.-s Zhao, Fuel 294 (2021).
[49] S. Xue, X. Zhang, R. Huang, H. Zhuang, C. Xue, Dalton Trans. (2008) 4296–4302, https://doi.org/10.1039/b804943b.
[50] S. Cai, M. Mayyas, M.G. Saborio, M.B. Ghasemian, J. Tang, T. Daeneke, J. Han, A. A. Esmailpour, F.-M. Allioux, K. Kalantar-Zadeh, J. Mater. Chem. C. 8 (2020) 16593–16602.
[51] F. Hoshyargar, J. Crawford, A.P. O'Mullane, J. Am. Chem. Soc. 139 (2017) 1464–1471.
[52] T. Gan, S. Handschuh-Wang, W. Shang, X. Zhou, Langmuir 38 (2022) 14475–14484.
[53] H.-D. Xiao, H.-L. Ma, C.-S. Xue, W.-R. Hu, J. Ma, F.-J. Zong, X.-J. Zhang, F. Ji, Diam. Relat. Mater. 14 (2005) 1730–1734.

Lin Peng is currently a doctoral student jointly trained by Beijing University of Chemical Technology and Beijing Institute of Nanoenergy and Nanosystems, Chinese Academy of Sciences. Her research interests include triboelectric nanogenerators, self-powered sensing systems, flexible electronic material and energy materials.

Zhong Lin Wang received his Ph.D. from Arizona State University in physics. He now is the Hightower Chair in Materials Science and Engineering, Regents' Professor, Engineering Distinguished Professor and Director, Center for Nanostructure Characterization, at Georgia Tech. Prof. Wang has made original and innovative contributions to the synthesis, discovery, characterization and understanding of fundamental physical properties of oxide nanobelts and nanowires, as well as applications of nanowires in energy sciences, electronics, optoelectronics and biological science. His discovery and breakthroughs in developing nanogenerators established the principle and technological roadmap for harvesting mechanical energy from the environment and biological systems for powering personal electronics. His research on self-powered nanosystems has inspired the worldwide effort in academia and industry for studying energy for micro-nano-systems, which is now a distinct disciplinary in energy research and future sensor networks. He coined and pioneered the field of piezotronics and piezophototronics by introducing piezoelectric potential gated charge transport process in fabricating new electronic and optoelectronic devices. Details can be found at: www.nanoscience.gatech.edu.

Liqun Zhang is a professor of Beijing University of Chemical Technology. His research interests focus on rubber science and technology, polymer nanocomposites, bio-based polymeric materials and so on. He has received various famous awards such as National Outstanding Youth Foundation, Changjiang Scholar Professor of Ministry of Education of China, Sparks-Thomas sci-tech award of Rubber Division of American Chemical Society, Science of Chemical Engineering of Japan (SCEJ) Research award, and Morand Lambla Award of International Polymer Processing Society. He has published over 300 peer-reviewed papers, and has given over 60 plenary/keynote/invited lectures in international conferences.

Xia Cao is currently a distinguished professor at the University of Science and Technology Beijing, and a professor at the Beijing Institute of Nanoenergy and Nanosystems, Chinese Academy of Sciences. Her main research interests include energy materials, nanogenerator, energy conversion and storage, flexible electronic sensor, and self-powered system.